Enhancement of Superconducting T_c (33 K) by Entrapment of FeSe in Carbon Coated Au−$Pd_{17}Se_{15}$ Nanoparticles

Sukhada Mishra,[†,⊥] Kai Song,[‡,⊥,∥] Kartik C. Ghosh,[§] and Manashi Nath[†,*]

[†]Department of Chemistry, Missouri University of Science and Technology, Rolla, Missouri 65409, United States, [‡]Materials Research Centre, Missouri University of Science and Technology, Rolla, Missouri 65409, United States, and [§]Physics, Astronomy and Material Science Department, Missouri State University, Springfield MO 65897, USA. [⊥]These authors contributed equally. [∥]Present address: FEI Company, 5350 NE Dawson Creek Drive, Hillsboro, Oregon 97124, USA.

ABSTRACT FeSe has been an interesting member of the Fe-based superconductor family ever since the discovery of superconductivity in this simple binary chalcogenide. Simplicity of composition and ease of synthesis has made FeSe, in particular, very lucrative as a test system to understand the unconventional nature of superconductivity, especially in low-dimensional models. In this article we report the synthesis of composite nanoparticles containing FeSe nanoislands entrapped within an *ent*-FeSe-$Pd_{16}Se_{15}$−Au nanoparticle and sharing an interface with $Pd_{17}Se_{15}$. This assembly exhibits a significant enhancement in the superconducting T_c (onset at 33 K) accompanied by a noticeable lattice compression of FeSe along the ⟨001⟩ and ⟨101⟩ directions. The T_c in FeSe is very sensitive to application of pressure and it has been shown that with increasing external pressure T_c can be increased almost 4-fold. In these composite nanoparticles reported here, immobilization of FeSe on the $Pd_{17}Se_{15}$ surface contributes to increasing the effect of interfacial pressure, thereby enhancing the T_c. The effect of interfacial pressure is also manifested in the contraction of the FeSe lattice (up to 3.8% in ⟨001⟩ direction) as observed through extensive high-resolution TEM imaging. The confined FeSe in these nanoparticles occupied a region of approximately 15−25 nm, where lattice compression was uniform over the entire FeSe region, thereby maximizing its effect in enhancing the T_c. The nanoparticles have been synthesized by a simple catalyst-aided vapor transport reaction at 800 °C where iron acetylacetonate and Se were used as precursors. Morphology and composition of these nanoparticles have been studied in details through extensive electron microscopy.

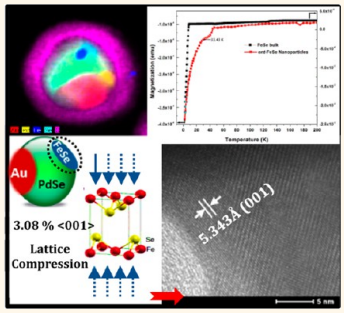

KEYWORDS: FeSe nanoparticles · FeSe nanostructures · T_c enhancement · interfacial pressure

The discovery of superconductivity in a simple binary compound, FeSe at 8 K[1] enriched the family of Fe-based superconductors which started with Hosono's report of superconductivity in the layered iron oxypnictide LaFePO.[2] All these Fe-based superconductors contain analogous crystal structures where the Fe_2X_2 (X = P, As, and Se) layer containing tetrahedrally coordinated Fe is the main structural ingredient.[2,3] In the pnictogen based superconducting families, the cationic layers are alternately stacked between the anionic Fe_2X_2 layers, while in FeSe, neutral layers of interconnected $FeSe_4$ tetrahedra are stacked along the *c*-direction.[4,5] In the layered structure, $FeSe_4$ tetrahedra is distorted from its regular shape and the layers are loosely bound to each other through van der Waals interactions giving rise to an inhomogeneous compressibility in the structure.[6,7] Interestingly, when an external pressure of 1.5 GPa was applied to FeSe, a 10% reduction in the unit cell parameters led to the contraction of interlayer separation (in the *c*-direction) and enhanced the T_c from 8 to 36.7 K.[7,8] Among all the iron based superconductors, FeSe exhibits largest pressure-sensitivity and shows the highest enhancement of T_c under external pressure. The enhancement in T_c and corresponding structural transitions in FeSe under the application of an external pressure has been studied extensively following the initial report by Cava and coworkers.[6−9] On the basis of several reports, it was evident that the application of pressure compresses the crystal structure of tetragonal FeSe along the *c*-axis (*i.e.*, layer stacking direction) thereby, decreasing the unit cell volume. The anion height also plays an important role in the enhancement of T_c under high pressure. As pressure is applied, the selenium height decreases leading to an enhancement of T_c.[6] As the pressure is

* Address correspondence to nathm@mst.edu.

Received for review August 14, 2013 and accepted February 4, 2014.

Published online February 04, 2014
10.1021/nn404262v

amplified further from 11.5 to 16 GPa, the tetragonal phase of FeSe irreversibly transforms into more densely packed hexagonal phase which destroys superconductivity.[8] The influence of the anion height toward T_c in FeSe is also evident from another report by Song *et al.* who have shown that increasing the Se height in the vicinity of twin boundaries in stoichiometric FeSe thin films leads to a suppression of the superconducting T_c.[10] T_c in FeSe could be also significantly altered by introducing a spacer layer, *e.g.*, $A_xFe_{2-y}Se_2$ family of compounds showed a T_c of 30−46 K, while recently isolated $Li_x(NH_2)_y(NH_3)_{1-y}FeSe$ exhibited a T_c as high as 43 K.[11,12]

The effect of applying external pressure can be also induced through chemical doping (*chemical pressure*),[13] confining morphology or by introduction of an interphase.[14] Among these the effect of confined morphology on the superconducting properties including T_c deserves special mention. Previously researchers have reported that the superconducting parameters can be altered upon nanostructuring, *e.g.*, a 5% enhancement in T_c and 160−400 times higher H_c for zero-dimensional In nanoparticles;[15,16] 60−120 times higher H_c for Pb nanoparticles,[17] enhanced T_c and critical field for TaC nanoparticles;[18] and a size dependence of the superconducting transition for an array of YBCO nanowires.[19] Recently, few reports on FeSe micro and nanostructures suggest that a slight enhancement in T_c (≈10 K) was observed for FeSe wires,[20] and nanoparticles[21] where the nanoparticles also showed signs of a higher transition at ∼30 K.[21] Following this study, another report claimed that a dramatic enhancement of onset $T_c \approx 53$K[22] could be obtained by growing single unit cell layer of FeSe over $SrTiO_3$ (STO) substrate, and they predicted that the T_c can be further increased up to 80 K by modifying the STO substrate. This enhancement of T_c was attributed to an enhanced electron−phonon coupling at the FeSe/STO interphase. Recently, we have also synthesized superconducting FeSe nanocables through chemical vapor deposition (CVD) catalyzed by Au−Pd nanoparticles.[14] During this study we observed that the FeSe near the Pd−interface showed a significant lattice compression along the *c*-direction. This lattice contraction was maximum near the interface and decreased further along the FeSe length and expectedly the effect on T_c was very minimal.[14] Hence, we redesigned the experiments in an attempt to confine the FeSe nanostructure growth entirely near the catalyst (Pd) interface, such that the entire FeSe is under lattice compression. In this article we describe the synthesis of composite [FeSe−$Pd_{17}Se_{15}$−Au]@C nanoparticles (200−250 nm in diameter) where the *entrapped* FeSe (*ent*−FeSe) shares an interface with $Pd_{17}Se_{15}$ and occupies a region of 15−25 nm near the interface. Magnetic characterization showed that an ensemble of these nanoparticles was superconducting with a T_c onset at ∼33K, which is four times higher than that for bulk FeSe.

RESULTS AND CHARACTERIZATION

Synthesis of Au−$Pd_{17}Se_{15}$−FeSe (*ent*-FeSe) Composite Nanoparticles. The composite nanoparticles containing *ent*-FeSe was synthesized by catalyst aided chemical vapor deposition, following a procedure reported previously.[14] An Au:Pd (3:2) alloy was used as a catalyst for the FeSe nanostructure growth, while iron(III) tris-(acetylacetonate) [$Fe(acac)_3$] and Se were used as precursors (see Supporting Information) in a chemical vapor deposition assembly. The flow rate of the carrier gas (N_2) played a definitive role in controlling the morphology of the products. Details of the synthesis procedure have been provided in the Materials and Methods section.

The as-synthesized product (a golden brown film covering the Si substrate) was further characterized through powder X-ray diffraction (pxrd), scanning electron microscopy (SEM) and energy dispersive spectrometry (EDS) to investigate the morphology, elemental compositions and superconducting transition temperature (T_c). Scanning transmission electron microscopy (STEM) and high resolution transmission electron microscopy (HRTEM) was performed after transferring the product from the Si substrate to a carbon coated Cu TEM grid. Magnetic properties were measured by superconducting quantum interference device (SQUID), while Raman, Mössbauer, and X-ray photoelectron spectroscopies (XPS) were also performed to get a better insight into the elemental composition.

Morphology and Structure of the Nanoparticles. The pxrd of the as-synthesized product as shown in Figure 1a confirmed the presence of tetragonal FeSe (JCPDS card number, 04−001−9129) along with cubic $Pd_{17}Se_{15}$ (JCPDS card number, 01−074−6160) and Au in the brownish deposit covering the Si substrate. As the nanoparticles were dispersed as a thin film on Si substrate, owing to small amount of scattering values and high obstructive scattering noise from the Si substrate, weak intensities were obtained in pxrd pattern. However, it was observed that the (001) line for FeSe showed a slight shift for the peak maxima resulting in the lattice parameter *c* being 5.28 Å (reported value is 5.52 Å), while the (101) peak was also shifted to yield a *d*-spacing of 3.02 Å (reported value is 3.09 Å). These shifts in the pxrd peak positions indicated that there might be some contraction of the FeSe lattice in the nanoparticles. The thickness of the FeSe region was estimated to be ∼25 nm from the (001) line using the Scherrer formula.[23] Peaks due to the Si substrate and SiO_2 was discernible in the pxrd pattern. SEM characterization was performed directly with the product spread over the Si substrate. Figure 1b demonstrates the low magnification SEM image, showing homogeneous layer of nanoparticles covering the Si substrate.

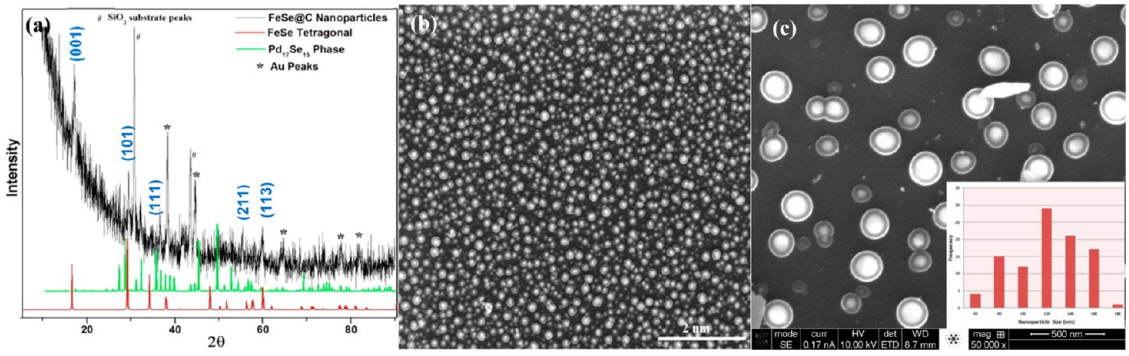

Figure 1. (a) XRD pattern of the product showing the presence of tetragonal FeSe and cubic $Pd_{17}Se_{15}$ phase along with the Au peaks. (b) SEM image demonstrating the yield of the nanoparticles on the Si substrate. (c) Magnified SEM image of the nanoparticles, showing the presence of core−shell type of morphology of the nanoparticles. Inset shows the diameter distribution of the nanoparticles.

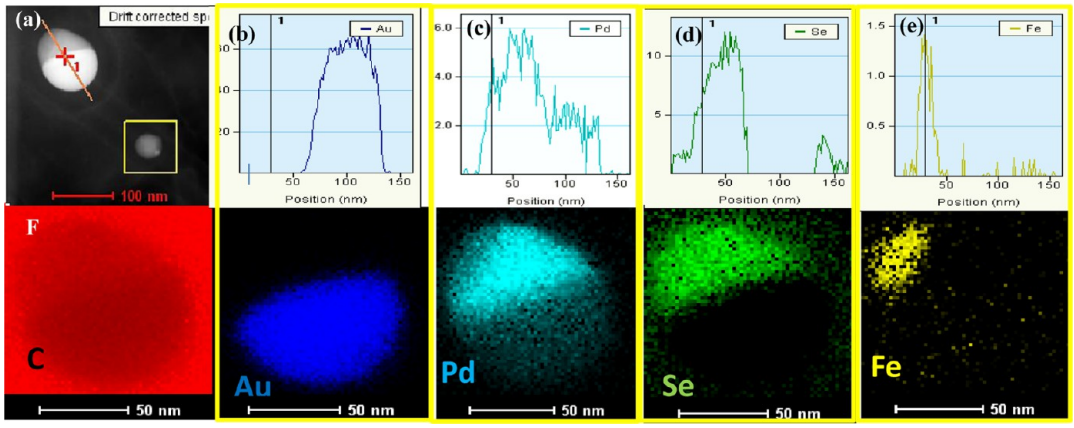

Figure 2. (a) Dark-field STEM image of a single nanoparticle on which elemental line scan was performed across the line. (b−e) Elemental line scans showing distribution of Au, Pd, Se, Fe. The bottom panels in (b)−(e) show the mapping of corresponding element in the nanoparticle demonstrating the presence of segregated Au, Pd/Se rich, and Fe/Se rich regions. (f) Elemental mapping for C confirming formation of the shell.

Figure 1c shows a magnified view of these nanoparticles demonstrating core−shell type of distinctive morphology. From the histogram analysis collected from several low magnification SEM images, the sizes of the nanoparticles were observed to be in the range of 200−250 nm (inset of Figure 1c).

Reactions were carried out at various temperatures to study the evolution of the product morphology. It was observed that the nanoparticle morphology was similar to that observed by heating the catalyst particles at low temperature (600 °C) which exhibited a distinct segregation of the bimetallic catalyst into Au and Pd/Se-rich zones, thereby forming an eye-ball kind of morphology (Supporting Information Figure S1). The phase segregation was also carried over to the composite nanoparticles obtained in the current study. EDAX analysis from these nanoparticles revealed that individual nanoparticles were composed of Fe, Se, Pd, Au and C. To get a better insight into the regional presence of the constituent elements, the nanoparticles were subjected to detailed line scan and elemental mapping analysis in the STEM mode of TEM as shown in Figure 2(b-f), where the line scan was performed on a single nanoparticle as shown in the dark-field STEM image in Figure 2a. The microscope operation parameters and technical specifications have been provided in details in the Materials and Methods section. The presence of Au as shown in Figure 2b was demonstrated in the bright contrast region (Figure 2a). The occurrence of Pd and Se in the middle region confirmed the formation of a Pd/Se alloy (Figure 2c, d). Interestingly, the Fe signal picks up from the other end of the nanoparticle, opposite to the Au catalyst region (Figure 2e). The bottom panels in Figure 2b−e show the elemental mapping performed on the same particle. The carbon signal was enriched on the entire particle (Figure 2f), suggesting the presence of carbon as a coating on the nanoparticle. The Au, Pd−Se, and Fe−Se regions were reflective of the line scan analysis which illustrated that the Fe-rich region was adjacent to the Pd-rich zone and away from the Au. Extensive elemental mapping and line scan analyses were performed on several nanoparticles and also by tilting individual nanoparticles in the TEM imaging process to get the global picture.

Owing to the spherical morphology and complex elemental composition of the as synthesized nanoparticles,

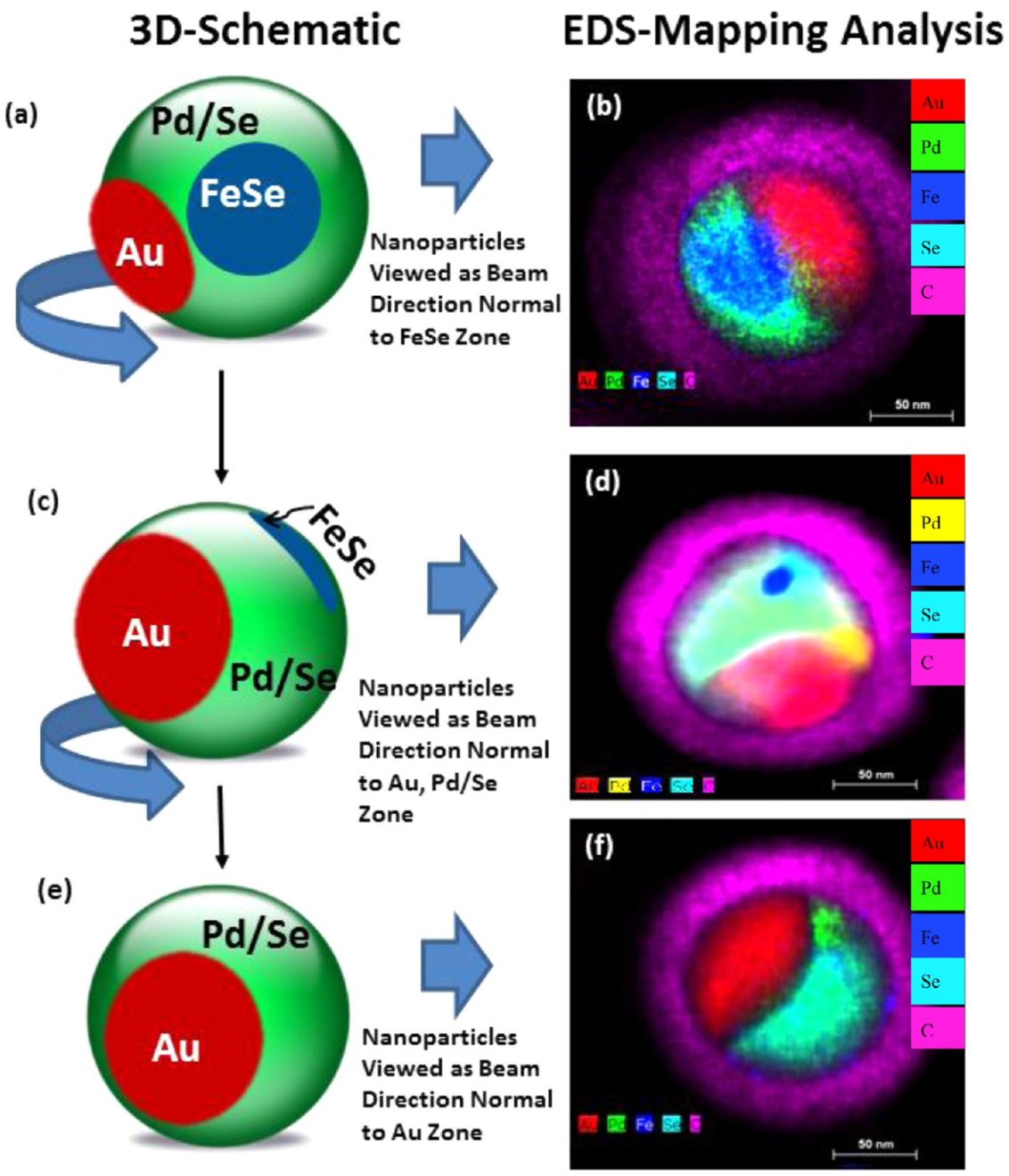

Figure 3. (a, c, and e) Graphical representations of the *ent*-FeSe-$Pd_{17}Se_{15}$−Au@C nanoparticles "as seen" from different view directions during STEM imaging. EDS mapping performed by tilting the nanoparticle thereby having (b) FeSe region perpendicular to the direction of electron beam, (d) FeSe concentrated at the edges, (f) facing the Au region with FeSe concealed at the back. Element color codes for (b), (c), (f) have been provided on the right side for clarity.

extensive EDS mapping experiments in TEM were performed to focus at various locations of the nanoparticles through tilting the TEM sample stage. Elemental mapping performed after tilting the nanoparticles (up to ±20°) confirmed that the FeSe regions were always adjacent to the Pd-region of the catalyst and away from the Au-rich zone. As TEM produces 2-dimensional imaging results, spherical 3-dimensional models were created to better visualize the results of the mapping studies. These analyses gave an approximate idea about the 3-dimensional architecture of these composite nanoparticles. Figure 3 shows a schematic representation comparing the experimental elemental mapping with the probable compositional architecture of these nanoparticles as shown in Figure 3a,c,e. Depending on the viewing direction, the FeSe region can be very prominent right on top of the nanoparticles as shown in the experimental mapping image in Figure 3b, while Figure 3a shows the probable morphology. The same nanoparticle if viewed atop the Au region (which can be achieved by tilting the sample stage), the FeSe region was shifted to the very edge (Figure 3d showing

the experimental mapping analysis, while 3c shows the schematic representation) or was totally masked by the overlying Pd−Se and Au regions (Figure 3e, corresponding to the experimental mapping image in Figure 3f). From these detailed analysis, it was confirmed that the *ent*-FeSe in these nanoparticles was indeed confined between the $Pd_{17}Se_{15}$ on one side and the carbon shell on the other side, and had a large interface with the $Pd_{17}Se_{15}$.

The composition of the nanoparticles and the shell was also confirmed through XPS analysis where elemental analysis and the quantification results (Supporting Information Figure S2) confirmed the presence of C, Fe and Se along with the trace amounts of Au and Pd. Upon careful observation, it was evident that after sputtering for about 15 min (which removes ~10 nm from the surface), intensity of the carbon signal reduced drastically accompanied by decrease in atomic weight percentage from 76.76% to 54.92%, which confirmed that the shell composition is primarily carbonaceous. Raman spectroscopy analysis of these composite nanoparticles, which showed the *D* band and *G* band at 1315.83 and 1581.63 cm^{-1}, respectively, also confirmed the presence of carbonaceous shell in the form of disordered carbon ($I_D/I_G \sim 3.08$).

The composition of the FeSe phase in the nanoparticles was also ascertained through Mössbauer spectroscopy which showed features characteristic of tetragonal FeSe (Supporting Information Figure S3). Mössbauer has been known to be more sensitive in distinguishing different coordination environments and spin state of Fe. Typically, the hexagonal FeSe with the NiAs structure type and containing octahedral coordination of Fe shows a distinctively different Mössbauer spectra with higher chemical shift (~0.8 mm/s) than the tetragonal FeSe which has 4-coordinated Fe.[8,24] The Mössbauer spectra collected from an ensemble of these composite nanoparticles containing *ent*-FeSe at room temperature showed a doublet with isomer shift of 0.42 mm/s and a quadruple splitting of 0.29 mm/s (Figure S3), which corresponds well with that of bulk tetragonal FeSe. The low intensity of the signal might be attributed to the very low concentration of FeSe in each nanoparticle and accordingly in the entire sample. Nevertheless, the close similarity between the spectra obtained from the nanoparticles and bulk tetragonal FeSe illustrates the phase purity of FeSe in these composite nanoparticles. It also signifies that the *ent*-FeSe crystallized within the composite nanoparticles is almost free of hexagonal FeSe impurity, since with the current Mössbauer setup, impurities even less than 1% can be identified in the spectra.

High-Resolution TEM Characterization. Extensive HRTEM analysis was carried out to investigate the structural details of individual regions in these nanoparticles. Figure 4a−d shows the HRTEM images acquired from the different regions (R1−R4) of *ent*-FeSe-$Pd_{17}Se_{15}$−Au@C nanoparticle. Figure 4a shows a bright field TEM image of a single *ent*-FeSe-$Pd_{17}Se_{15}$−Au@C nanoparticle, showing three distinct regions of different contrasts. As confirmed from the line mapping and elemental analysis the darkest region denoted by R1 corresponds to the Au-region, while the middle region of the nanoparticles represented the uniform Pd/Se phase (R2 in the image). It was also evident that the FeSe regions were concentrated at the periphery of the nanoparticles in R3 and R4 regions, respectively. Figure 4b shows HRTEM image of the Au region showing lattice spacing of 2.35 Å corresponding to the [111] planes of Au. The SAED obtained from the Au region as shown in the inset of Figure 4b, also confirmed the presence of single crystalline Au and the diffraction spots could be indexed to $(1\bar{1}1)$ and (220) planes. Figure 4c shows the HRTEM image obtained from the R4 region, where the lattice fringes and electron diffraction obtained from Fast Fourier Transform (FFT) (shown in inset) confirmed the presence of tetragonal FeSe. The zone axis being [111], the spots could be indexed to (001), (010) and (101) lattice planes of tetragonal FeSe. Interestingly, the calculated *d*-spacing along these planes corresponds to 5.343, 3.469, and 2.81 Å, which demonstrated 3.08% contraction along *c*-direction (reported value of 5.51 Å), 8.22% compression along ⟨010⟩ (reported value of 3.77 Å) and 10.79% compression along ⟨101⟩ (reported value of 3.15 Å) directions, respectively. Extensive HRTEM images obtained from the FeSe regions near the edge (Region R3) of the nanoparticles also showed the existence of lattice compression of ~9.01% in ⟨101⟩ planes (Supporting Information Figure S4). Figure 4d shows the HRTEM obtained from the Pd-rich central zone of the nanoparticles (designated as R2 in the nanoparticle shown in Figure 4a). The lattice fringes observed in this region corresponds to the [211] and [210] planes of $Pd_{17}Se_{15}$. Inset shows the FFT generated ED pattern which confirmed the phase. For the HRTEM analysis, Si single crystals were used as calibration sample for lattice spacing accuracy and all calculations for lattice spacing were done by counting at least 15 lattice planes. From the extensive HRTEM and SAED analysis, it was evident that the FeSe in these nanoparticles showed appreciable lattice compression which might be attributed to the effect of restricted growth (entrapment) and the presence of an interface between the growing FeSe and $Pd_{17}Se_{15}$ as has been observed earlier in the FeSe nanocables.[14] However, it should be noted here that the lattice compression is uniform over the entire FeSe region (~15−25 nm) in these nanoparticles. This is in contrast to the FeSe nanocables reported earlier where the FeSe lattice shows maximum contraction near the interface with $Pd_{17}Se_{15}$ and it relaxes back to its original form as FeSe moves away from the interface.[14]

FeSe Lattice Compression and Its Effect on T_c. The pressure sensitivity of the superconducting T_c in FeSe has been

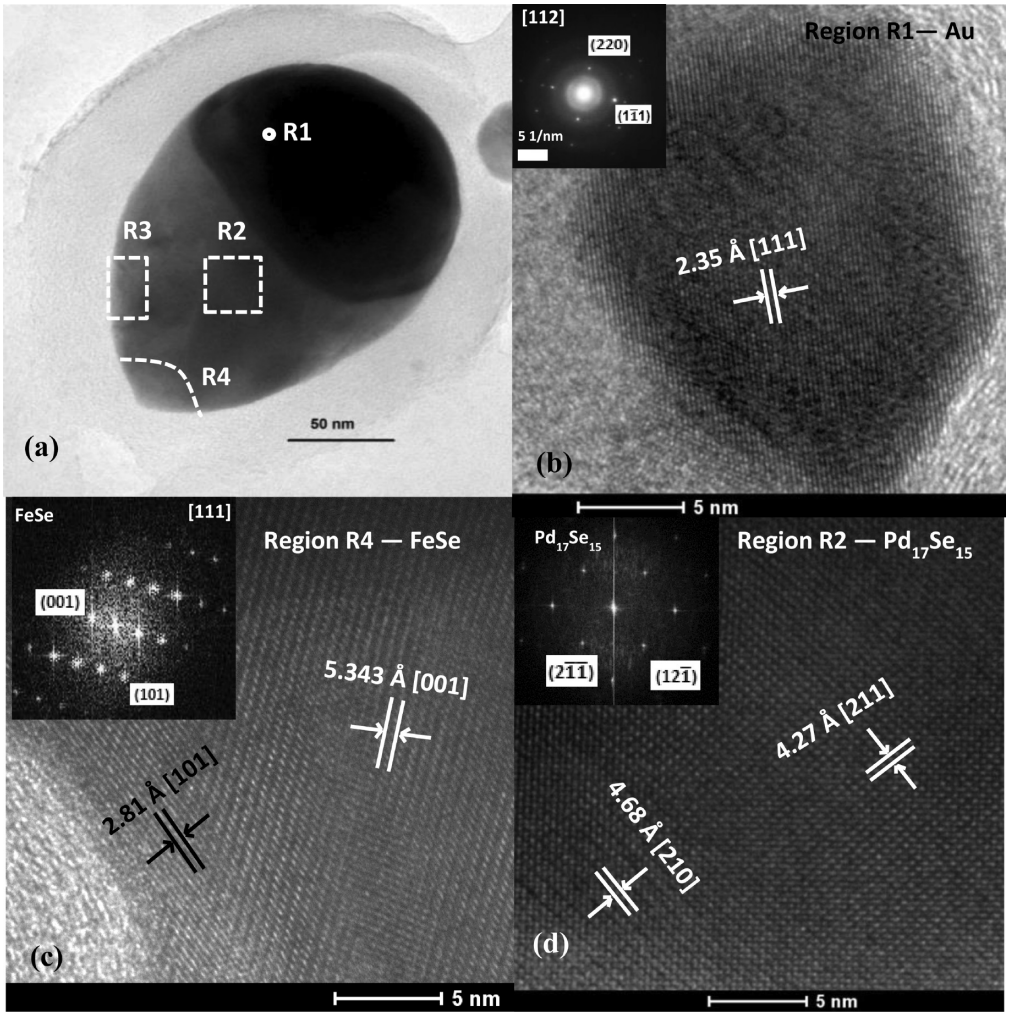

Figure 4. (a) Low-magnification image of the *ent*-FeSe-PdSe-Au@C nanoparticle showing different regions (R1-Au, R2-PdSe, R3 and R4-FeSe). (b) HRTEM image of the Au region (R1), having *d*-spacing of 2.35 Å corresponding to (111) planes. (c) FeSe region at the edges of nanoparticle (shown by R4) with lattice fringes corresponding to (001) planes showing a spacing of 5.343 Å. Inset shows the FFT generated ED pattern. (d) Lattice fringes obtained from the $Pd_{17}Se_{15}$ region (R2) at the middle of the nanoparticle showing a lattice spacing of 4.27 Å for the (211) planes and 4.68 Å for (210) lattice planes. Inset demonstrates the FFT generated ED pattern.

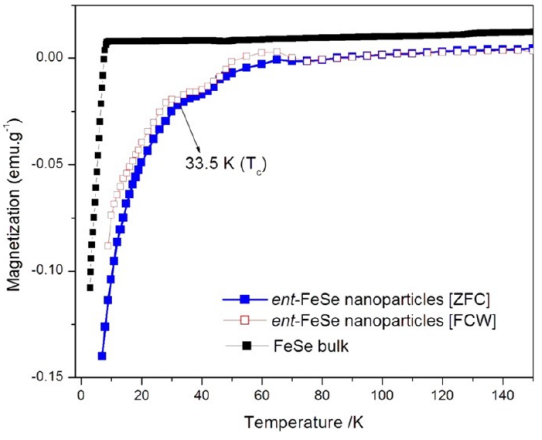

Figure 5. ZFC and FCW plot of magnetization *vs* temperature for the *ent*-FeSe-$Pd_{17}Se_{15}$—Au@C nanoparticles showing the onset of the superconductivity at ≈33K.

the most prominent among the Fe-based superconductors. Following research by various groups it was concluded that both hydrostatic and nonhydrostatic application of pressure caused the similar kind of effect in FeSe, *viz.*, enhancement of T_c.[7,8,25,26] Hence, it was evident that the T_c enhancement was not specific to the method of application or pressure. As the FeSe lattice contracted along the *c*-axis, the anion height decreased leading to a closer packing of the FeSe layers. This led to an enhancement of the T_c. In the composite nanostructures reported here, the FeSe lattice shows a considerable compression along the ⟨001⟩ and ⟨101⟩ directions.

To study the effect of lattice compression of FeSe on the superconducting transition temperature (T_c), magnetization was measured as a function of temperature under zero field cooled and field cooled conditions using SQUID magnetometer. The measurements were performed on an ensemble of nanoparticles spread on the Si substrate. Figure 5 shows the plot of magnetization [both zero field cooled cooling (ZFC) and field

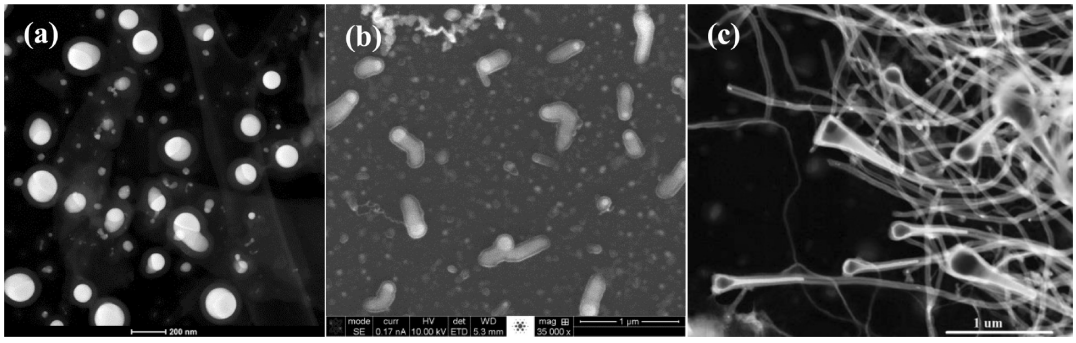

Figure 6. STEM/SEM images capturing the product morphology under different flow rates for the carrier gas (N_2): (a) dark-field STEM image of the composite nanoparticles containing *ent*-FeSe formed at 80 sccm flow rate; (b) SEM image of anisotropic 1-dimensional nanostructures grown at 120 sccm; (c) dark-field STEM image of the FeSe nanocables grown at 180 sccm.

cooled warming (FCW) data] as a function of temperature for the *ent*-FeSe nanoparticles as compared with bulk FeSe powder under an applied field of 1000 Oe. Superconducting transition for nanoparticles was clearly observed in both the ZFC and FCW plots with a T_c onset at approximately 33 K which was higher than that of bulk FeSe (T_c = 8 K) measured under similar conditions. The magnetization data for the nanoparticle ensemble was normalized simply with respect to mass of the sample dispersed over Si. The exact mass of *ent*-FeSe in these ensembles could not be precisely determined since FeSe accounts for only a fraction of the total mass of these nanoparticles. The magnetization of a blank Si substrate was also measured under similar conditions and used as a reference. As expected, the Si substrate by itself did not demonstrate any appreciable transition; however, it did show a noise around 50 K, which was also observed in the other magnetization plots (Supporting Information Figure S5). It should be noted here that both the ZFC and FCW plots show an abnormality in the region 40 − 70 K which is reminiscent of the broad hump observed with blank Si. Hence, the feature around 50 K was attributed mainly due to background noise arising from condensation of trapped oxygen. The magnetization data from the nanoparticle ensemble was heavily masked by the diamagnetic background from both the Si substrate and the carbonaceous shell. Nevertheless, such an enhancement in T_c can be ascribed as the effect of FeSe lattice compression caused by the interfacial and morphological pressure in these nanoparticles. The transition, however, appears to be broad. This can be explained by the particle size distribution and the observation that the actual size of FeSe within these nanoparticles can vary from particle to particle. Accordingly, the confinement and the extent of compression of FeSe lattice can be different between particles. While the majority of the nanoparticles reported in this study contained *ent*-FeSe occupying a region of ~15−25 nm, there were few bigger nanoparticles with much larger area of *ent*-FeSe. In bigger nanoparticles, as the FeSe occupies a wider space, the lattice compression may not be uniform and it can actually spring back to its original form away from the interface, thereby reducing the pressure effect. As the lattice relaxes back, the T_c will be closer to the bulk value. This is in accordance with the observation made by the current authors in FeSe nanocables, where reducing lattice compression along the length of FeSe led to bulk-like T_c.[14] The resistivity measurements which are typically performed by fabricating the electrical contacts on tightly packed powder pellets could not be conducted because of the nature of the sample. Currently efforts are underway to conduct the resistivity measurements by making electrical contacts through lithographic patterning on a film of nanoparticles.

Recently, there have been other reports of T_c enhancement in FeSe either by application of pressure, intercalation of spacer layer, or by growing extremely thin FeSe thin films (about 1 unit cell thick).[7,8,11,27,28] In these composite nanoparticles, we show another way of enhancing the T_c by applying interfacial pressure and confining the growth. The catalyst composition and structure might play a significant role in introducing the interfacial pressure, and our current efforts are focused on using Pd nanostructures as catalysts for FeSe growth. Efforts are also underway to decrease the thickness of the FeSe region further which may lead to even higher T_c.

Mechanism of Formation. The morphology of the FeSe-$Pd_{17}Se_{15}$−Au nanostructures was dependent on the CVD reaction conditions including gas flow rate of the carrier gas and the catalysts composition. To elucidate the growth mechanism, the authors performed several experiments by varying the reaction parameters. It was realized that only Pd was the active part in the bimetallic catalyst, while using Au nanoparticles alone failed to produce any such nanostructures as reported here. The enhanced catalytic activity of Pd under these conditions can be understood by studying the binary phase diagrams of Pd−Fe system.[29] From the binary Fe−Pd phase diagram, it can be seen that Fe has considerable solubility in Pd and forms solid solution of α-Fe and Pd in the low Pd region in the temperature range of 600−815 °C. In the high Pd content region,

it forms alloys of the composition FePd and $FePd_3$ below 790 and 820 °C, respectively. The Au−Fe binary phase diagram, on the other hand, shows that Fe has limited miscibility with Au within the range of the reaction temperature.[30] Hence, in the present case, $Fe(acac)_3$ sublimes and pyrolyzes under the reaction condition, and the Fe-rich vapors generated thereby dissolve and diffuse preferentially within the Pd region of the bimetallic catalyst. As Se vapors are fed into the system, the Pd end of the catalyst gets converted into $Pd_{17}Se_{15}$, while the dissolved Fe is converted to FeSe, which precipitates out from one end of the active catalyst region (Pd). The limited solubility of Fe and Se in Au makes the Au end of the catalyst inactive and immobilized at the non-FeSe terminal of the composite nanoparticle. It should be noted here that in the composite nanoparticle there was no evidence of elemental Fe and the formation reaction of FeSe was complete.

The effect of carrier gas flow on the morphology of the product was investigated by performing the CVD reactions under different flow rates of N_2. Under lower gas flow rate (80 sccm, sccm = standard cubic centimeter per minute), the product contained mostly nanoparticle as shown in Figure 6a. As the gas flow was increased to 120 sccm, the product morphology changed from spherical nanoparticles to elongated rod-shaped nanostructures, while still maintaining the heterocomposition, as shown in Figure 6b. Under much higher gas flow (180 sccm), FeSe@C nanocables were formed as has been reported previously (Figure 6c).[14] This kind of dependency of product morphology on the carrier gas flow rate is reminiscent of other observations where higher flow rates typically yields more anisotropic growth and 1-dimensional nanostructures. In the present case, as the flow rate increases, the feedstock of carbonaceous species into the reaction chamber also increases manifold (attributed to the carbon content in the acetylacetonate precursor), thereby aiding in the rapid longitudinal growth of the shell, thus forming the nanofibers under high flow rate.

CONCLUSION

In conclusion, we have developed a protocol for the synthesis of composite *ent*-FeSe-$Pd_{17}Se_{15}$−Au nanoparticles where the FeSe is entrapped between $Pd_{17}Se_{15}$ and the carbonaceous shell. This assembly leads to a considerable contraction of the FeSe lattice thereby leading to an almost 4-fold enhancement with the onset of superconducting T_c at 33 K. The effect on T_c is similar to that obtained by subjecting tetragonal FeSe to an external pressure which was also accompanied by a compression of the lattice.[7,8] This report illustrates that the effect of external pressure can be induced through interfacial pressure and morphology confinement in these nanostructures. By carefully controlling the composition of the catalyst and reducing the thickness of the FeSe layer further to only few unit cell layers thick, it might be possible to increase the T_c even more.

MATERIALS AND METHODS

Synthesis of *ent*-FeSe-$Pd_{17}Se_{15}$−Au Composite Nanoparticles. The composite nanoparticles containing *ent*-FeSe were grown on a Si substrate (Si quest international) by chemical vapor deposition. These Si substrates were cut into pieces of 1 × 1 cm^2 and prewashed with 2-propanol and acetone in order to remove dirt particles. No extra precautionary step was taken to remove the native oxide layer. The substrates were then sputtered coated with Au−Pd (3:2) for 120 s creating a thick layer (approximately 100 nm) of Au−Pd over the substrates.

A chemical vapor deposition with a horizontal tube furnace assembly was utilized to synthesize the composite nanoparticles. Si substrates were kept at the central region of the horizontal furnace at 800 °C. With the help of a mass flow controller, the reaction assembly was maintained at a continuous N_2 flow of 80 sccm. Iron(III) acetylacetonate (99% purity, STREM chemicals) and selenium shots (1−3 mm, amorphous, 99.999%) were chosen to be the precursors for Fe and Se, respectively. Selenium shots were positioned at 400 °C, while the $Fe(acac)_3$ was kept at a 180 °C region. Initially, The $Fe(acac)_3$ and Se were kept outside the heating zone by pushing the ceramic liner to the extreme left. Once the central zone of the furnace was reached the reaction temperature (800 °C), the ceramic liner was pushed to the right such that the Se and $Fe(acac)_3$ were at 400 and 180 °C, respectively. This steps were crucial for reproducibility of the reaction, as it avoids the sublimation and escape of the reactants (Se and $Fe(acac)_3$ vapors) before the Au/Pd catalyst reaches the melting temperature. The reaction was conducted out for 30 min, and the furnace was cooled down at the rate of 8 °C/min. After the reaction was completed, we observed a golden brown deposition on the Si substrate.

Characterization of the *ent*-FeSe Composite Nanoparticles. *Powder X-ray Diffraction.* The product was characterized without any subsequent purification through powder X-ray diffraction (Philips X-Pert) using Cu Kα (1.5418 Å) radiation. Because the product formed a very thin layer on the Si substrate, the pxrd was collected at grazing angles in thin film geometry (GI mode with Göbel mirrors).

Electron Microscopy Characterizations. Scanning electron microscope imaging was performed using FEI Helios NanoLab 600 FIB/FESEM) directly onto the Si substrate covered with the nanocables. The EDS line scan in Figure 2 was conducted on an FEI Tecnai F20 TEM operated at 200 keV in STEM mode. The probe current is 1.2 nA with a spot size of less than 2 nm. The convergence angle is 13 mrad and the camera length is 30 mm for dark field imaging. This scope is equipped with an Oxford ultrathin (UTW) window EDS detector, which allows detection of carbon. The X-ray transmission efficiency for carbon with this window is 42%.

The EDS mappings in Figure 3 were performed on an FEI Tecnai Osiris TEM operated at 200 keV in STEM mode. The probe current is 1 nA with a spot size of less than 1 nm. The convergence angle is 10.3 mrad and the camera length is 200 mm for HAADF imaging. This scope is equipped with a high brightness gun and four windowless SDD EDS detectors, which allow easy detection of light elements such as carbon and boron with high precision. Moreover, the symmetrical layout of four SDD detectors surrounding the sample minimizes the loss of X-ray signal at tilting.

TEM images were obtained on FEI Tecnai F20 and Tecnai Osiris TEM operating at 200 kV. The deposition on Si substrate was both scratched and dispersed in an acetone solution to

prepare the TEM sample. A drop of the "as prepared" solution was placed onto a carbon coated TEM grid and dried in air prior to TEM imaging and EDS.

High resolution TEM in Figure 4 was obtained with the Tecnai Osiris operated at 200 keV with a probe current of 2.5 nA. The Fast Fourier Transform (FFT) patterns generated from the lattice fringes clearly demonstrated the crystalline character of the individual regions, *i.e.*, Au, $Pd_{17}Se_{15}$ and FeSe.

Magnetic Characterizations. Magnetization data was collected from a SQUID magnetometer. The Si-substrate containing the *ent*-FeSe composite nanoparticles was loaded into a gel cap and was inserted into the magnetometer with the help of standard sample loader. The diamagnetic signal from the gel cap was collected separately and subtracted as a background from the signal obtained from the sample. The ZFC data was obtained after cooling the sample down to ~2 K under 0 magnetic field and then by measuring the magnetization during the warming up cycle. The FCW data was collected by cooling the sample down from room temperature to 2 K under an applied field of 500 Oe and then collecting the warming up data under an applied field. The magnetization of a blank Si substrate which was heat treated under conditions (similar to that for FeSe nanocable growth) was also collected and used as a reference.

Mössbauer Spectroscopy. Samples for collecting Mössbauer spectra were prepared by transferring the deposited powder from top of the Si substrate to a transparent tape which was loaded into the window of a 0.5 in. diameter sample holder. The powdered sample was spread on the tape such that it formed a uniform covering in the orifice. ^{57}Fe Mössbauer experiments were performed in transmission geometry at room temperature over 10 days period using a conventional constant acceleration spectrometer and a γ-ray source of ^{57}Co (50 mCi) in a Rh matrix. Velocity calibration and isomer shifts are given with respect to α-Fe foil at room temperature. The Mössbauer data was analyzed by Lorentzian line fitting using RECOIL software.[31]

X-ray Photoelectron Spectrometry. Elemental quantification was performed on a Kratos Axis 165 Photoelectron Spectrometer. The Si substrate containing an ensemble of the FeSe@C nanocables was analyzed both before and after sputtering. Sputtering was performed for 20 min, which removed approximately 20 nm layer from the substrate.

Conflict of Interest: The authors declare no competing financial interest.

Acknowledgment. The authors would like to acknowledge the Materials Research Center, for equipment usage, Dr. Switzer, Dr. Koza for their help with magnetic characterizations, Dr. Brow for help in Raman spectroscopic analysis and Dr. Choudhury for the Mössbauer spectral analysis. This research was funded by University of Missouri Research Board.

Supporting Information Available: XPS analysis, SEM imaging of the catalysts nanoparticles at low temperature, HRTEM analysis of FeSe region in nanoparticles, magnetization behavior of Si substrate and Mössbauer spectra of the composite nanoparticles. This material is available free of charge *via* the Internet at http://pubs.acs.org.

REFERENCES AND NOTES

1. Hsu, F. C.; Luo, J. Y.; Yeh, K. Y.; Chen, T. K.; Huang, T. W.; Wu, P. M.; Lee, Y. C.; Huang, Y. L.; Chu, Y. Y.; *et al.* Superconductivity in the PbO-Type Structure α-FeSe. *Proc. Natl. Acad. Sci. U.S.A.* **2008**, *105*, 14262–14264.
2. Kamihara, Y.; Hiramatsu, H.; Kawamura, R.; Yanagi, H.; Kamiya, T.; Hosono, H. Iron-Based Layered Superconductor: LaFePO. *J. Am. Chem. Soc.* **2006**, *128*, 10012–10013.
3. Hosono, H. Layered Iron Pnictide Superconductors: Discovery and Current Status. *J. Phys. Soc. Jpn.* **2008**, *77* (Suppl. C), 1–8 and references cited therein.
4. Büchner, B.; Hess, C. Iron-Based Superconductors: Vital Clues from a Basic Compound. *Nat. Mater.* **2009**, *8*, 615–616.
5. Margadonna, S.; Takabayashi, Y.; McDonald, M. T.; Kasperkiewicz, K.; Mizuguchi, Y.; Takano, Y.; Fitch, A. N.; Suarde, E.; Prassides, K. Crystal Structure of the New $FeSe_{1-x}$ Superconductor. *Chem. Commun.* **2008**, 5607–5609.
6. Okabe, H.; Takeshita, N.; Horigane, K.; Muranaka, T.; Akimitsu, J. Pressure-Induced High-T_c Superconducting Phase in FeSe: Correlation between Anion Height and T_c. *Phys. Rev. B* **2010**, *81*, 205119(1−6).
7. Margadonna, S.; Takabayashi, Y.; Ohishi, Y.; Mizuguchi, Y.; Takano, Y.; Kagayama, T.; Nakagawa, T.; Takata, M.; Prassides, K. Pressure Evolution of the Low-Temperature Crystal Structure and Bonding of the Superconductor FeSe (T_c = 37 K). *Phys. Rev. B* **2009**, *80*, No. 064506.
8. Medvedev, S.; McQueen, T. M.; Troyan, I. A.; Palasyuk, T.; Eremets, M. I.; Cava, R. J.; Naghavi, S.; Casper, F.; Ksenofontov, V.; Wortmann, G.; *et al.* Electronic and Magnetic Phase Diagram of β-$Fe_{1.01}Se$ with Superconductivity at 36.7 K Under Pressure. *Nat. Mater.* **2009**, *8*, 630–633.
9. Bendele, M.; Amato, A.; Conder, K.; Elender, M.; Keller, H.; Klauss, H.-H.; Luetkens, H.; Pomjakushina, E.; Raselli, A.; Khasanov, R. Pressure Induced Static Magnetic Order in Superconducting $FeSe_{1-x}$. *Phys. Rev. Lett.* **2010**, *104*, No. 087003.
10. Song, C. L.; Wang, Y.-L.; Jiang, Y.-P.; Wang, L.; He, K.; Chen, X.; Hoffman, J. E.; Ma, X.-C.; Xue, Q.-K. Suppression of Superconductivity by Twin Boundaries in FeSe. *Phys. Rev. Lett.* **2012**, *109*, No. 137004.
11. Ying, T. P.; Chen, X. L.; Wang, G.; Jin, S. F.; Zhou, T. T.; Lai, X. F.; Zhang, H.; Wang, W. Observation of Superconductivity at 30~46 K in $A_{(x)}Fe_2Se_2$ (A = Li, Na, Ba, Sr, Ca, Yb and Eu). *Sci. Rep.* **2012**, *2*, 42610.1038/srep00426.
12. Burrard-Lucas, M.; Free, D. G.; Sedlmaier, S. J.; Wright, J. D.; Cassidy, S. J.; Hara, Y.; Corkett, A. J.; Lancaster, T.; Baker, P. J.; Blundell, S. J.; *et al.* Enhancement of the Superconducting Transition Temperature of FeSe by Intercalation of a Molecular Spacer Layer. *Nat. Mater.* **2013**, *12*, 15–19.
13. Zinth, V.; Jorhendt, D. The Interplay of Electron Doping and Chemical Pressure in $Ba(Fe_{1-y}Co_y)_2As_{1-x}P_x)_2$. *EPL* **2012**, *98*, 57010-p1–57010-p6.
14. Mishra, S.; Song, K.; Koza, J. A.; Nath, M. Synthesis of Superconducting Nanocables of FeSe Encapsulated in Carbonaceous Shell. *ACS Nano* **2013**, *7*, 1145–1154.
15. Li, W. H.; Yang, C. C.; Tsao, F. C.; Wu, S. Y.; Huang, P. J.; Chung, M. K.; Yao, Y. D. Enhancement of Superconductivity by the Small Size Effect in In Nanoparticles. *Phys. Rev. B* **2005**, *72*, No. 214516.
16. Wu, F. Y.; Yang, C. C.; Wu, C. M.; Wang, C. W.; Li, W.-H. Superconductivity in Zero-Dimensional Indium Nanoparticles. *J. Appl. Phys.* **2007**, *101*, 09G111–113.
17. Zolotavin, P.; Guyot-Sionnest, P. Meissner Effect in Colloidal Pb Nanoparticles. *ACS Nano* **2010**, *4*, 5599–5608.
18. Fukunaga, A.; Chu, S.; McHenry, M. E. Synthesis, Structure and Superconducting Properties of Tantalum Carbide Nanorods and Nanoparticles. *J. Mater. Res.* **1998**, *13*, 2465–2471.
19. Xu, K.; Heath, J. R. Long, Highly-Ordered High-temperature Superconductor Nanowire Arrays. *Nano Lett.* **2008**, *8*, 3845–3849.
20. Ozaki, T.; Deguchi, K.; Mizuguchi, Y.; Kawasaki, Y.; Tanaka, T. Fabrication of Binary FeSe Superconducting Wires by Diffusion Process. *J. Appl. Phys.* **2012**, *111*, No. 112620.
21. Chang, C. -C.; Wang, C.-H.; Wen, M.-H.; Wu, Y.-R.; Hsieh, Y.-T.; Wu, M.-K. Superconductivity in PbO-Type Tetragonal FeSe Nanoparticles. *Solid State Commun.* **2012**, *152*, 649–652.
22. Wang, Q. Y.; Li, Z.; Zhang, W.-H.; Zhang, Z.-C.; Zhang, J.-S.; Li, W.; Ding, H.; Ou, Y.-B.; Deng, P.; Chang, K.; *et al.* Interface-Induced High-Temperature Superconductivity in Single Unit-Cell FeSe Thin Films on $SrTiO_3$. *Chin. Phys. Lett.* **2012**, *29*, No. 037402.
23. Patterson, A. L. The Scherrer Formula for X-Ray Particle Size Determination. *Phys. Rev.* **1939**, *56*, 978–981.
24. Reddy, K. V.; Chetty, S. C. Mossbauer Studies on the Fe-Se System. *Phys. Status Solidi A* **1975**, *2*, 585–592.
25. Uhoya, W.; Tsoi, G.; Vohra, Y.; Wolanyk, N.; Muralidhara Rao, S.; Wu, M.-K.; Weir, S. Simultaneous Measurement of Pressure Evolution of Crystal Structure and Superconductivity in $FeSe_{0.92}$ Using Designer Diamonds. *EPL* **2012**, *99*, 26002-p1–26002-p6.

26. Braithwaite, D.; Salce, B.; Lapertot, G.; Bourdarot, F.; Marin, C.; Aoki, D.; Hanfland, M. Superconducting and Normal Phases of FeSe Single Crystals at High Pressure. *J. Phys.: Condens. Matter* **2009**, *21*, No. 232202.
27. Tan, S.; Zhang, Y.; Xia, M.; Ye, Z.; Chen, F.; Xie, X.; Peng, R.; Xu, D.; Fan, Q.; Xu, H.; *et al.* Interface-Induced Superconductivity and Strain-Dependent Spin Density Waves in FeSe/$SrTiO_3$ Thin Films. *Nat. Mater.* **2013**, *12*, 634–640.
28. He, S.; He, J.; Zhang, W.; Zhao, L.; Liu, D.; Liu, X.; Mou, D.; Ou, Y. B.; Wang, Q. Y.; Li, Z.; *et al.* Phase Diagram and Electronic Indication of High-Temperature Superconductivity at 65 K in Single-Layer FeSe Films. *Nat. Mater.* **2013**, *12*, 605–610.
29. Raub, E.; Beeskow, H.; Loebich, O. The Iron-Palladium Phase Diagram below 950 °C. *Z. Metallkd.* **1963**, *54*, 549–552.
30. Okamoto, H.; Massalski, T. B.; Swartzendruber, L. J.; Beck, P. A. The Au-Fe (Gold-Iron) System. *Bull. Alloy Phase Diagrams* **1984**, *5*, 592–600.
31. Recoil software: Lagarec, K.; Rancourt, D. G. *Nucl. Instrum. Methods Phys. Res., Sect. B* **1997**, *129*, 266.